**ORIGINAL PAPER**

# Co-localization of microstructural damage and excessive mechanical strain at aortic branches in angiotensin-II-infused mice

Lydia Aslanidou[1] · Mauro Ferraro[1] · Goran Lovric[2,3] · Matthew R. Bersi[4,5] · Jay D. Humphrey[4] · Patrick Segers[6] · Bram Trachet[1,6] · Nikos Stergiopulos[1]

## Abstract

Animal models of aortic aneurysm and dissection can enhance our limited understanding of the etiology of these lethal conditions particularly because early-stage longitudinal data are scant in humans. Yet, the pathogenesis of often-studied mouse models and the potential contribution of aortic biomechanics therein remain elusive. In this work, we combined micro-CT and synchrotron-based imaging with computational biomechanics to estimate in vivo aortic strains in the abdominal aorta of angiotensin-II-infused ApoE-deficient mice, which were compared with mouse-specific aortic microstructural damage inferred from histopathology. Targeted histology showed that the 3D distribution of micro-CT contrast agent that had been injected in vivo co-localized with precursor vascular damage in the aortic wall at 3 days of hypertension, with damage predominantly near the ostia of the celiac and superior mesenteric arteries. Computations similarly revealed higher mechanical strain in branching relative to non-branching regions, thus resulting in a positive correlation between high strain and vascular damage in branching segments that included the celiac, superior mesenteric, and right renal arteries. These results suggest a mechanically driven initiation of damage at these locations, which was supported by 3D synchrotron imaging of load-induced ex vivo delaminations of angiotensin-II-infused suprarenal abdominal aortas. That is, the major intramural delamination plane in the ex vivo tested aortas was also near side branches and specifically around the celiac artery. Our findings thus support the hypothesis of an early mechanically mediated formation of microstructural defects at aortic branching sites that subsequently propagate into a macroscopic medial tear, giving rise to aortic dissection in angiotensin-II-infused mice.

## 1 Introduction

Degenerative conditions of the aorta, such as progressive aneurysmal dilatation, acute dissection, or catastrophic rupture, are influenced strongly by the biomechanical loads that act on the vessel wall. Importantly, dissection and rupture occur when the intramural mechanical stress exceeds the strength of the wall (Humphrey and Holzapfel 2012; Vorp 2007), with dissections involving a tearing of intimal/medial layers that allows blood to enter the wall. An associated progressive separation within the medial layer can create a false channel parallel to the true lumen that may or may not re-enter the aorta. Mechanical stimuli are thought to be key contributors to the initiation of aneurysms and dissections, not just their progression (Manopoulos et al. 2018). Estimation of the mechanical stresses/strains within the vessel wall via biomechanical simulations thus represents a promising approach for risk stratification (Farotto et al. 2018; Leemans

✉ Lydia Aslanidou
lydia.aslanidou@epfl.ch

1 Institute of Bioengineering, École Polytechnique Fédérale de Lausanne, Lausanne, Switzerland

2 Centre d'Imagerie BioMédicale, École Polytechnique Fédérale de Lausanne, Lausanne, Switzerland

3 Swiss Light Source, Paul Scherrer Institute, Villigen, Switzerland

4 Department of Biomedical Engineering, Yale University, New Haven, USA

5 Department of Biomedical Engineering, Vanderbilt University, Nashville, USA

6 bioMMeda, Ghent University, Ghent, Belgium

et al. 2016) and patient-specific interventional management (Bonfanti et al. 2017; Chen et al. 2016; Perrin et al. 2016). Simulations can also help enhance our hitherto limited understanding of the pathogenesis and early arterial remodeling that is characteristic of aneurysms and dissections, thus leading to an improved prognostic capability and therapeutic design. Computational models of the biosolid and biofluid mechanics suggest, for example, that pressure-induced hotspots of elevated normal wall stress (Nathan et al. 2011) and flow-induced hotspots of elevated wall shear stress (Chi et al. 2017) occur around the branching regions of the aortic arch, where initial dissecting tears often manifest. A continuing limitation of computational models, however, is the lack of validation due to the paucity of longitudinal patient data, particularly during early stages of the disease. Animal models can therefore serve as invaluable complements to human studies.

Chronic infusion of the vasoconstrictive peptide angiotensin-II (AngII) in atherosclerosis-prone mice is a well-accepted model for dissecting aortic aneurysms (Daugherty and Cassis 2004; Trachet et al. 2015b). The observed lesions develop within hours to days in the suprarenal abdominal aorta and are caused by a medial tear that is often accompanied by marked dissection and intramural hematoma (Daugherty et al. 2000; Saraff et al. 2003). A number of studies investigated roles of hemodynamic loads in this AngII-induced model of dissection (Cao et al. 2010; Goergen et al. 2010; Trachet et al. 2011), motivated by earlier suggestions of the likely importance of mechanical stresses in the etiology (Sho et al. 2004; Wang et al. 2001). An important subsequent experimental finding, however, was the histomorphometric identification of transmural disruptions in the vicinity of orifices at major side branches in the late stages of the disease, namely after 28 days of AngII infusion (Gavish et al. 2012, 2014). Although this finding focused subsequent attention on the potential biomechanical vulnerability of branch points (Trachet et al. 2014, 2017), the precise role of biomechanics in the initiation and early progression of AngII-induced lesions has remained elusive.

Our continuing search for biomechanical mechanisms must nevertheless build on prior studies. Numerous imaging modalities, including in vivo magnetic resonance imaging, high-frequency ultrasound and ex vivo panoramic digital image correlation, have been used to estimate regional biomechanics in the AngII-infused murine abdominal aorta (Adelsperger et al. 2018; Favreau et al. 2012; Genovese et al. 2012; Goergen et al. 2011). Biaxial mechanical testing has also shed light on the solid mechanics of the mouse aortic wall prior to and during AngII infusion (Bersi et al. 2017; Laroumanie et al. 2018). Mouse-specific fluid dynamics simulations have been used to understand flow patterns in the true aortic lumen either prior to AngII infusion (Trachet et al. 2011) or in the late stages of disease

development when a false lumen is present (Ford et al. 2011; Phillips et al. 2017). Mouse-specific fluid–solid interaction (FSI) simulations have shown the distribution of principal stresses in a healthy mouse aorta (Trachet et al. 2015a), but computational efforts focusing on the early stage of AngII-induced lesions with appropriate mouse-specific validation are lacking.

We have previously performed ex vivo synchrotron-based imaging of AngII-induced dissecting aneurysms by means of phase contrast X-ray tomographic microscopy (PCXTM), which yielded 3D datasets of the aortic wall at 6.5 μm isotropic resolution (Trachet et al. 2014, 2017, 2018). We found that dissections starting as medial microruptures can be visualized ex vivo due to a fortuitous discovery: the micro-computed tomography (micro-CT) contrast agent injected into the mice in vivo (prior to euthanasia) infiltrated the aortic wall intra vitam to form microleaks that appeared as white aggregates. The advantage of such microleaks is that they can be analyzed in 3D along the entire vessel and therefore offer a much more accurate and complete assessment of vascular damage than what can be obtained by traditional slice-by-slice 2D histology—an arduous, expensive, and invasive procedure. Consistent with earlier histological findings (Gavish et al. 2012, 2014), the microleaks occurred mainly near the ostia of suprarenal side branches, with a particularly high incidence around the celiac and superior mesenteric arteries. It is expected that the preferential localization of these microruptures is intricately linked to the regional mechanics. Aiming to test this hypothesis, we introduced a custom automated morphing framework to map the non-pressurized, non-axially stretched, PCXTM geometry onto the pressurized, axially stretched in vivo micro-CT geometry (Ferraro et al. 2018). The output of this morphing scheme is a mouse-specific structural finite element simulation under pressurization and axial stretch. In this way, this synchrotron-based biomechanical modeling considers often-overlooked aspects of the native geometry—namely mouse-specific aortic wall thickness, minor aortic side branches and local axial stretch—that impact the location of hotspots in the computed in vivo aortic strain field (Ferraro et al. 2018). This morphing framework was only tested for a single mouse, however; thus, its general validity remained to be demonstrated.

The aim of this work is to test the hypothesis that the local mechanics at major abdominal side branches drive disease initiation in AngII-infused mice. To that end, we present an experimental–computational approach that was used to compare histopathological, imaging, and computational results regionally for AngII-infused and saline-infused control mice. We first verified that the infiltrated contrast agent can be used as a precursor for vascular damage and then compared the 3D distribution of infiltrated contrast agent to spatial hotspots of mechanical strain (obtained

with synchrotron-based biomechanics). Importantly, the associated mechanical strains were computed by comparing unloaded and temporally averaged loaded configurations of the abdominal aortic wall, not in vivo diastolic and systolic configurations. Finally, we further tested the hypothesis that load-induced delamination of the wall initiates at or near branch sites via synchrotron imaging of aortas that were mechanically tested ex vivo in the absence of complicating mechanical factors such as complex hemodynamics (Ford et al. 2011; Phillips et al. 2017) and perivascular tissue support (Ferruzzi et al. 2018), thus focusing on the effect of material and geometric heterogeneities at branch sites.

## 2 Methods

### 2.1 Animals

All procedures were approved by the Ethical Committee of Canton Vaud, Switzerland (EC 2647.2) and performed according to Directive 2010/63/EU of the European Parliament on the protection of animals used for scientific purposes. Twelve-week-old male ApoE-deficient mice on a C57BL/6 J background ($n = 10$) were infused for 3 days with AngII at a rate of 1000 ng/kg/min as previously described (Trachet et al. 2017). Age-, sex-, and strain-matched controls ($n = 6$) were infused for 3 days with 0.9% normal saline. All mice underwent a micro-CT scan (detailed below) just prior to euthanasia with a ketamine/xylazine cocktail (100 mg/kg and 15 mg/kg, respectively), and aortic tissue was collected immediately after euthanasia.

### 2.2 Imaging

#### 2.2.1 In vivo

The abdominal region was imaged using contrast-enhanced non-gated micro-CT on the third day of AngII infusion. The contrast agent (ExiTron nano 12,000; Miltenyi Biotech, Germany) was injected into the lateral caudal vein at 4 mL/g body mass, and imaging was achieved using a Quantum FX micro-CT scanner (Caliper Life Sciences, USA). Anesthesia was maintained throughout scanning with an inhalation of 1.5% isoflurane. We used compressors that concentrate room air to oxygen levels between 85% and 91% (model: Sequal Integra E-Z Oxygen concentrator), which then deliver this concentrated air to the inhalation anesthesia system. The resulting DICOM images had an isotropic voxel size of 50 μm. The soft-tissue contrast of this technique delineates the blood-filled aortic lumen but is not sufficient for visualization of the aortic wall thickness. Resulting segmentations of the aorta from these (non-gated) scans represent an average of the systolic and diastolic geometries.

#### 2.2.2 Ex vivo

The abdominal aortas of the 10 AngII-infused and 6 saline-infused control mice were excised and fixed in 4% paraformaldehyde (PFA). The samples were then imaged at the TOMCAT beamline of the Swiss Light Source in the Paul Scherrer Institute, Villigen, Switzerland. Images were acquired in stacked scans with 6.5 μm isotropic resolution using differential phase contrast X-ray tomographic microscopy (PCXTM), as previously described (Trachet et al. 2014, 2017). This complementary imaging modality enables tissue contrast sufficient to quantify wall thickness and to segment small side branches off the aorta (Trachet et al. 2015c).

### 2.3 Histology

The reliability of local contrast agent distribution as a marker of vascular damage was first validated against targeted 2D histology. Briefly, after ex vivo PCXTM scanning, samples were processed and embedded in paraffin using standard histological procedures. We then followed procedures for PCXTM-guided histology that we introduced previously (Trachet et al. 2014). Namely, upon examination of the PCXTM dataset for each sample, we identify sites of contrast agent infiltration and serially section the embedded samples to obtain desired locations, including those with and without contrast agent as well as with and without branches. Slides were stained with hematoxylin–eosin (H&E) to assess general morphology: 214 slides from the 10 AngII-infused mice and 157 from the saline-infused control mice. Whereas eosin also stains erythrocytes red, a Martius, Scarlet and Blue (MSB) stain was used to assess fibrin within coagulated blood. Immunostaining identified macrophages (F4/80), continuity of the endothelial cell layer (CD31), and smooth muscle cells (α-smooth muscle actin, α-SMA). Pathophysiological observations in each slide were assessed by an investigator blinded from the PCXTM-guided histology.

### 2.4 Computational Analyses

We sought to assess mechanical strains locally along the abdominal aorta by comparing the loaded (micro-CT) and unloaded (PCXTM) configurations. Toward this end, semi-automatic segmentations of paired in vivo micro-CT and ex vivo PCXTM scans were performed using the image processing software Mimics (Materialise NV, Belgium). Preprocessing, meshing, and morphing were achieved using an integrated framework that has been described in detail elsewhere (Ferraro et al. 2018).

## 2.5 Preprocessing

Precise lengths of the aortic side branches could not be estimated from the micro-CT images; hence, we developed a consistent extension technique to mitigate effects of artificial stretching during the morphing simulation. Each side branch was numerically extended in proportion to a related length measured in the micro-CT model. For example, the distance between the celiac and superior mesenteric bifurcations was calculated in terms of the abscissa coordinate of the centerline in both the micro-CT and PCXTM scans (see Fig. 1d), which was clearly identifiable with both imaging modalities. The ratio between these two quantities provided an extension coefficient that multiplied the PCXTM side branch length to yield an extension length.

### 2.5.1 Meshing

The outer vascular surface in each PCXTM segmentation was discretized with an unstructured quadrilateral mesh. This mesh was then smoothed using a non-shrinking Taubin filter (passband 0.1, 100 smoothing iterations) and projected onto the mesh of the inner wall using a custom MATLAB code [the MathWorks, Inc., Natick, MA, USA, code available in the supplementary material for Ferraro et al. 2018]. The final result was an unstructured hexahedral solid mesh of the ex vivo geometry. Several meshes were autogenerated to ensure that the simulations were independent of the grids used; details of the final converged meshes, including the average, maximum, and minimum element edge lengths, are given in Table 1. Convergence could not be reached for only 1 of the 10 AngII-infused mice, mainly due to element distortions related to poor local element quality. Conversely, the collapsed ex vivo geometry hindered mesh generation for 4

**Table 1** Mesh size and edge lengths for the geometrical models

| Case | # Elements | Average edge length (μm) | Maximum edge length (μm) | Minimum edge length (μm) |
|---|---|---|---|---|
| *AngII-infused* | | | | |
| 1 | 713,952 | 10.1 | 45.0 | 1.0 |
| 2 | 267,808 | 17.2 | 113.0 | 1.7 |
| 3 | 275,464 | 18.4 | 59.3 | 2.4 |
| 4 | 303,740 | 15.4 | 152.0 | 4.2 |
| 5 | 245,692 | 20.3 | 60.0 | 6.1 |
| 6 | 332,784 | 13.9 | 84.8 | 4.5 |
| 7 | 833,212 | 9.6 | 39.3 | 0.9 |
| 8 | 254,472 | 19.6 | 89.4 | 4.5 |
| 9 | 916,660 | 9.6 | 34.0 | 1.5 |
| *Saline-infused* | | | | |
| 1 | 611,208 | 10.1 | 81.4 | 1.3 |
| 2 | 220,000 | 21.1 | 72.1 | 1.3 |

of 6 control mice. All of the five cases of poor mesh quality are shown in Fig. 8 of Appendix.

### 2.5.2 Morphing simulation setup

In order to estimate strains along the abdominal aorta, we developed a pointwise mapping scheme between the ex vivo PCXTM mesh (not stretched, not pressurized) and the in vivo micro-CT model (in vivo axial stretch and pressurized). To this end, we introduced a branch-based coordinate transformation in which a cylindrical parameterization was generated from a rectangular parametric space for each branch. This transformation was applied to both the micro-CT and PCXTM models, and a global displacement map was
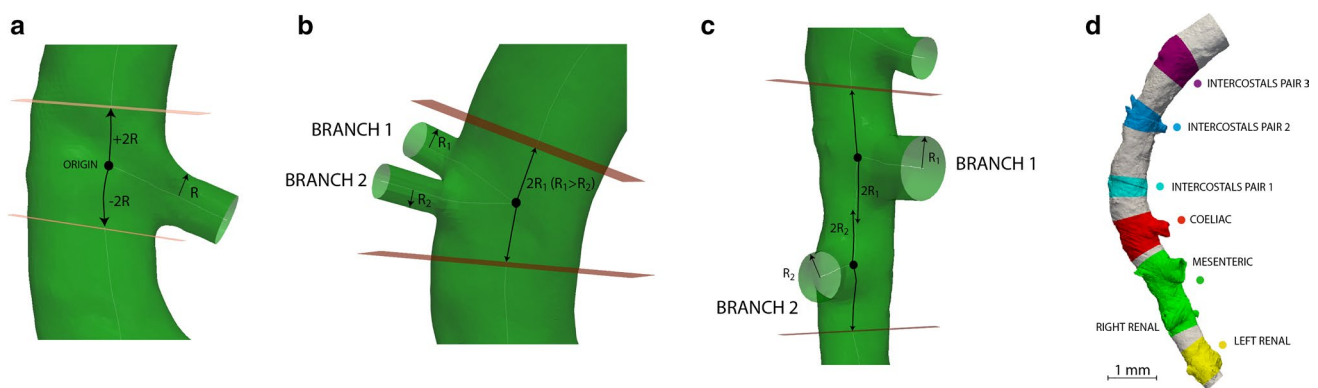


**Fig. 1** Schematic depiction of aortic partitioning at the level of ramifications. **a** Ramification with one daughter branch. Cutting planes intercept the abscissae at a distance of $\pm 2R$ with respect to the origin of the bifurcation. **b** Ramification with more than one daughter branch (from a common origin). Cutting planes intercept the abscissae at a distance of $\pm 2R$, where $R$ is the maximal of the daughter branches' radii. **c** Neighboring ramifications. If cutting planes applied for each ramification yield overlapping neighboring branching zones, the aortic regions are merged into a single branching segment. **d** Illustration of partitioned aorta in branching (colored) and non-branching (gray) segments

obtained by subtracting each nearest neighbor node in the micro-CT and PCXTM models, respectively.

The output of this novel method thus synthesized the hexahedral PCXTM mesh and the computed displacement map into a single structural finite element method (FEM)-based simulation of morphing. The morphing simulation was static and fully displacement controlled, allowing finite deformations. A nearly incompressible Arruda–Boyce constitutive model was used, with material parameters ($\mu = 24.358$ kPa, $\lambda_m = 1.01$) consistent with those used in a prior fluid–solid interaction simulation (Trachet et al. 2015a).

In order to co-localize results of the simulation with locations of microruptures that were identified using PCXTM imaging, the computed Eulerian strains were mapped back onto the ex vivo undeformed configuration, while artificial extensions of side branches were removed for visualization and excluded from the analysis.

## 2.6 Partitioning of the abdominal aorta

To allow consistent region-matched comparisons between aortic strains (computed from the FEM simulations) and vascular damage (observed from contrast infiltrations in PCXTM scans), the aorta was subdivided into branching and non-branching zones. Post-processing of data was achieved using the vascular modeling toolkit [VMTK, Orobix, Bergamo, Italy (The Vascular Modeling Toolkit website, www.vmtk.org), MATLAB (the MathWorks Inc., Natick, MA, USA), and the open-source code Paraview (Ayachit 2015)]. The VMTK subroutine *vmtkbifurcation referencesystems* was used to compute reference systems for the ramifications of the aortic tree, and Frenet–Serret tangents and abscissas were subsequently computed along the smoothed and resampled centerline of the simulated vessel geometry (subroutines *vmtkcenterlinenormals* and *vmtkcenterlineattributes*).

In the regions containing bifurcations, the aortic zone corresponding to a branch of radius R was delimited by two planes at a curvilinear centerline distance of $\pm 2R$ from the origin of the bifurcation (Fig. 1a). Planes laterally demarcating the branching segment were placed perpendicular to the centerline as defined by local Frenet–Serret tangents. In the case of multiple bifurcating branches from a common origin, the planes delimiting the segment were placed at a distance $2R_{max}$ above and below the origin, where $R_{max}$ was the maximum radius of the side branches (Fig. 1b). Adjacent ramifications were grouped with a single branching aortic segment if the curvilinear centerline distance between the originating points was not sufficient to define two separate segments without any overlap (Fig. 1c). Straight segments were then, by inference, defined as those lying between branching segments. Identical cutting planes were imposed on the ex vivo PCXTM scans to divide them into branching and non-branching segments. In most geometries, the

sectioning yielded 7 straight and 6 branching aortic segments, which are depicted in Fig. 1d.

## 2.7 Quantification of strain and 3D microstructural vascular damage

For each simulation, high values of strain were defined as $\geq 80\%$ of the maximal principal strain. For each aortic segment, the surface area A1 of high strain and the total surface area A2 of the aortic segment were exported into Paraview. We used a non-dimensional metric defined as the percentage of the A1/A2 ratio as a high strain index.
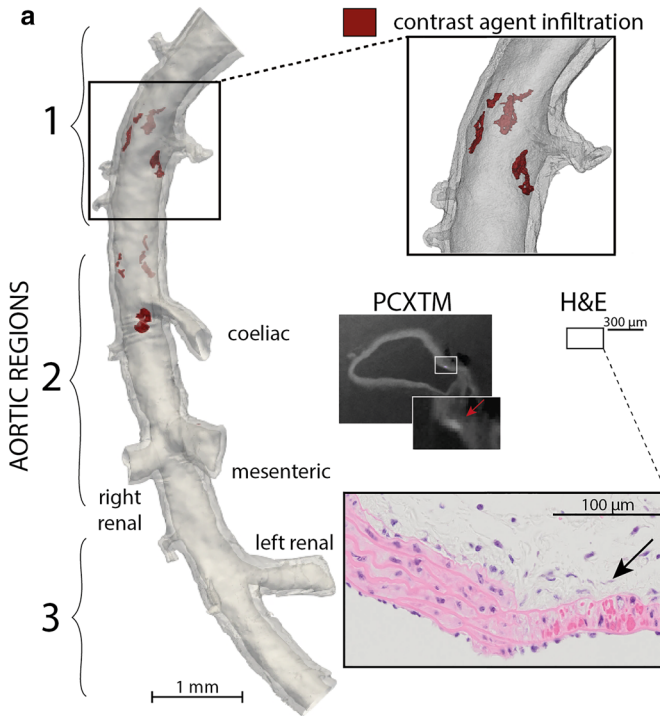
Microleaks of contrast agent within the aortic wall were segmented in the Mimics software. The quantified volume of contrast agent was subsequently partitioned using the same aortic segment definitions—hence, a volume of contrast agent, if present, was assigned to each aortic segment.

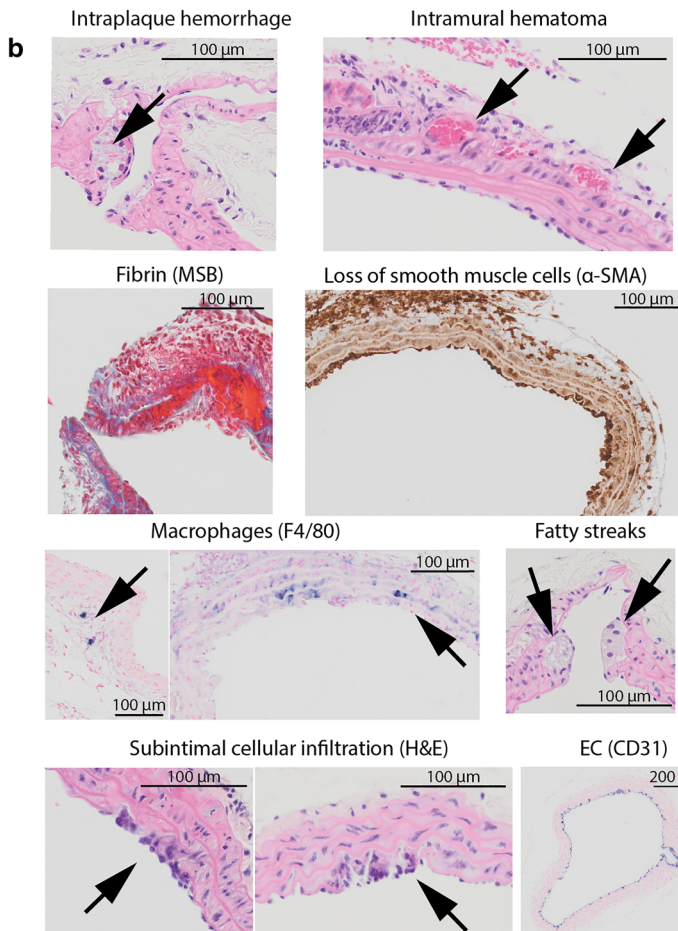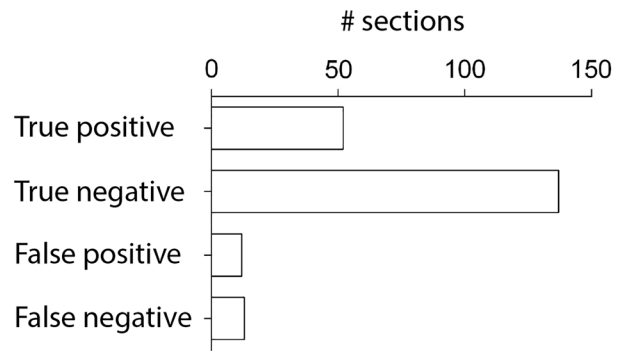## 2.8 Load-induced intramural delaminations ex vivo

Ex vivo biaxial mechanical testing can also be used to explore biomechanical mechanisms of aortic dissection in mouse models. In particular, load-induced intramural delaminations have been observed in aortas of mice that have a propensity to dissect in vivo (Ferruzzi et al. 2016; Laroumanie et al. 2018). Here, for the first time, we use synchrotron imaging (PCXTM at 6.5 µm isotropic resolution) to examine the abdominal aorta from male ApoE-deficient mice ($n = 4$) that were infused with AngII for 4 days (1000 ng/kg/min) and underwent ex vivo biaxial testing with concurrent optical coherent tomography (OCT) imaging, as previously described (Ferruzzi et al. 2016). The biaxial tests were carried out on freshly excised, non-fixed samples. Because the delaminations were observed in different regions (1 proximal descending aorta, 2 suprarenal abdominal aortas, and 1 infrarenal abdominal aorta), we used these data to further evaluate the role of branching regions as potential nucleation sites for dissection.

## 2.9 Statistical analysis

Differences in both mechanical strain and contrast agent infiltration between straight and branching segments were assessed with the nonparametric Mann–Whitney U test. Differences between AngII- and saline-infused mice in a given aortic region were evaluated with multiple t tests between the two groups with post-hoc Sidak–Bonferroni correction. For AngII-infused mice, a Kruskal–Wallis test with post hoc Dunn's testing for multiple comparisons was used to compare strain and contrast agent volumes between aortic locations and circumferential quadrants. Linear relationships between variables were assessed by the Pearson correlation.

**a**

AORTIC REGIONS

1

2

3

contrast agent infiltration

coeliac

mesenteric

right renal

left renal

PCXTM

H&E

300 μm

100 μm

1 mm

**b**

Intraplaque hemorrhage

100 μm

Intramural hematoma

100 μm

Fibrin (MSB)

100 μm

Loss of smooth muscle cells (α-SMA)

100 μm

Macrophages (F4/80)

100 μm

100 μm

Fatty streaks

100 μm

Subintimal cellular infiltration (H&E)

100 μm

100 μm

EC (CD31)

200 μm

**c**   Validation of 3D contrast agent with 2D histology

# sections

0       50       100       150

True positive

True negative

False positive

False negative

**d**   2D histology in aortic regions

**1. INTERCOSTAL REGION**

# sections

80

60

40

20

0

- Loss of VSMCs
- Intraplaque hemorrhage
- Subintimal infiltration
- Intramural hematoma
- Fibrin
- No finding

Ang-II   ctrls
Non-branching

Ang-II   ctrls
Branching

**2. PARAVISCERAL REGION**

# sections

80

60

40

20

0

- Loss of VSMCs
- Intraplaque hemorrhage
- Subintimal infiltration
- Intramural hematoma
- Fibrin
- No finding

Ang-II   ctrls
Non-branching

Ang-II   ctrls
Branching

**3. LEFT RENAL/INFRARENAL REGION**

# sections

80

60

40

20

0

- Loss of VSMCs
- Intraplaque hemorrhage
- Subintimal infiltration
- Intramural hematoma
- Fibrin
- No finding

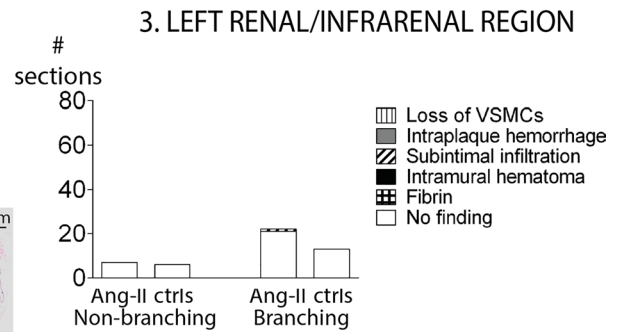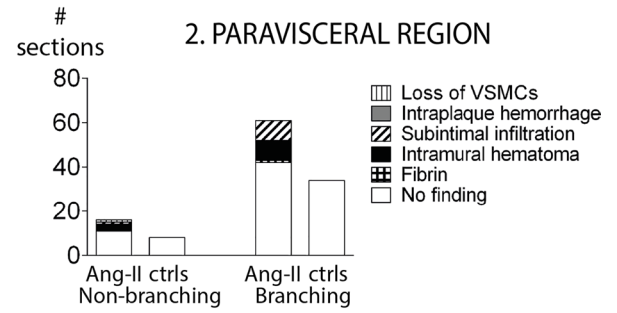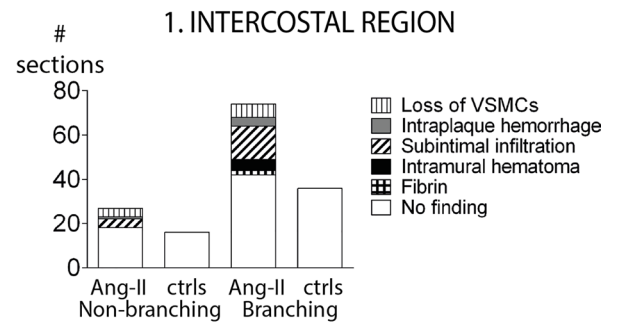Ang-II   ctrls
Non-branching

Ang-II   ctrls
Branching

◄**Fig. 2** Targeted image-guided histology. **a** 3D volume rendering of an abdominal aorta after 3 days of AngII infusion with zoomed suprarenal region (contrast agent in red). Note the correspondence between the ex vivo PCXTM image and targeted H&E section. The infiltrated contrast agent (red arrow) co-localizes in the zoomed H&E image with an intramural accumulation of red blood cells. This zoomed image also shows a transition of elastic laminae from 5 to 2 in the branching region. **b** Zoomed images of lesions (arrows) located on H&E, MSB and immunostained slides (α-SMA, CD31, F4/80). **c** Bar plot showing correspondence between the presence or absence of contrast agent in the wall and histopathological findings in AngII-infused mice. **d** Bar plots showing histopathological findings in AngII and saline-infused animals, in branching and non-branching sites of each aortic region shown in panel a

# 3 Results

## 3.1 Contrast agent infiltration in the wall is a proxy for microstructural damage

A 3D rendering of the abdominal aortic wall of a representative AngII-infused mouse shows regions of infiltrated contrast agent in red (Fig. 2a). Contrast agent was found in the aortic wall of all 10 AngII-infused mice but was absent in all aortic regions within the saline-infused control animals (cf. Fig. 3c). Despite the near normal gross morphology, H&E and immunostaining revealed a compromised structural integrity of the wall of the AngII-infused aortas in multiple locations (Fig. 2b). Intimal and intramural defects in the AngII-infused animals included a fragmented internal elastic lamina accompanied by subintimal cellular infiltration, intramural accumulation of red blood cells and fibrin, macrophage infiltration, and loss of vascular smooth muscle cells. In stark contrast, no histopathological findings arose in the saline-infused animals (Fig. 2d).

We also found good agreement between contrast agent localization and histopathological findings, as quantified in Fig. 2c. In 64% of the examined slides, the absence of contrast agent matched the absence of histopathological features (termed 'true negatives') while in 24% of the cases, contrast agent infiltration co-localized with histopathological findings (true positives). The main histological findings of the true positive cases were subintimal cellular infiltration and intramural hematoma (52% and 35% of true positives, respectively). False positives and false negatives, that is, a mismatch between contrast agent infiltration and microstructural damage, represented only 5% and 6% of the total cases, respectively. The finding that went mostly undetected with PCXTM was medial VSMC loss. (82% of all histologically identified instances were not accompanied by contrast agent infiltration.)

In the intercostal region of AngII-infused mice, the most prevalent histopathological feature was disruption of the intimal layer accompanied by subintimal cellular infiltration (46%), followed by loss of medial smooth muscle cells

(24%). Intramural hematoma (i.e., accumulation of red blood cells in the wall) was found in the outer lamellar layers at 7% of the branching sites but in none of the non-branching ones. In non-branching sites of the intercostal region, there was no lesion in 78% of the sections analyzed; this is in contrast to 61% absence for the branching sites. In the paravisceral aortic region, extending from above the celiac down to the right renal artery, the most prevalent lesions were intramural hematoma (50% of the observed lesions), followed by subintimal cellular infiltration (42%). The incidence of hematomas was similar in branching and non-branching sites (15% and 19% respectively, Fig. 2d). We observed that 50% and 55% of intramural hematomas in the intercostal and the paravisceral regions co-localized with medial macrophages. No macrophage infiltration was observed in the more distal aortic region, extending from above the left renal artery to the infrarenal aorta. The only observed lesion in this region was fibrin accumulation (4% of sections from AngII-infused mice).

## 3.2 Strain and contrast agent infiltration in the aorta: a macro-comparison

The structural FEM calculations of in vivo aortic strain obtained by implementing the morphing framework for 9 AngII and 2 saline-infused mice are shown in Fig. 3a. The corresponding ex vivo segmentations of the abdominal aortic wall and corresponding contrast agent microleaks—which serve as indicators of vascular damage—are shown in Fig. 3b. The mean value as well as the range of predicted values of strain was similar between those for the AngII- and saline-infused mice (Fig. 3c). There was also no significant correlation between minimum or maximum strain values and the total volume of contrast agent in the wall (Fig. 3d).

## 3.3 Strain and contrast agent infiltration in the aorta: branching and non-branching regions

In order to evaluate the distribution of strain—rather than its range of values—and to consistently assess the implication of branching regions on the strain map, we divided the aorta into branching and straight (non-branching) regions. Representative analysis of the abdominal aortic branching topology resulted in the partitioned geometry shown in Fig. 4 (center). For each mouse, the high strain index and volume of contrast agent infiltration were quantified within each straight and branching segment. Overall, the high strain index in the branching regions was significantly greater than in the straight regions ($P < 0.0001$, Fig. 4a). Similarly, the volume of contrast agent was significantly lower in straight regions than in branching regions ($P = 0.0028$, Fig. 4b).
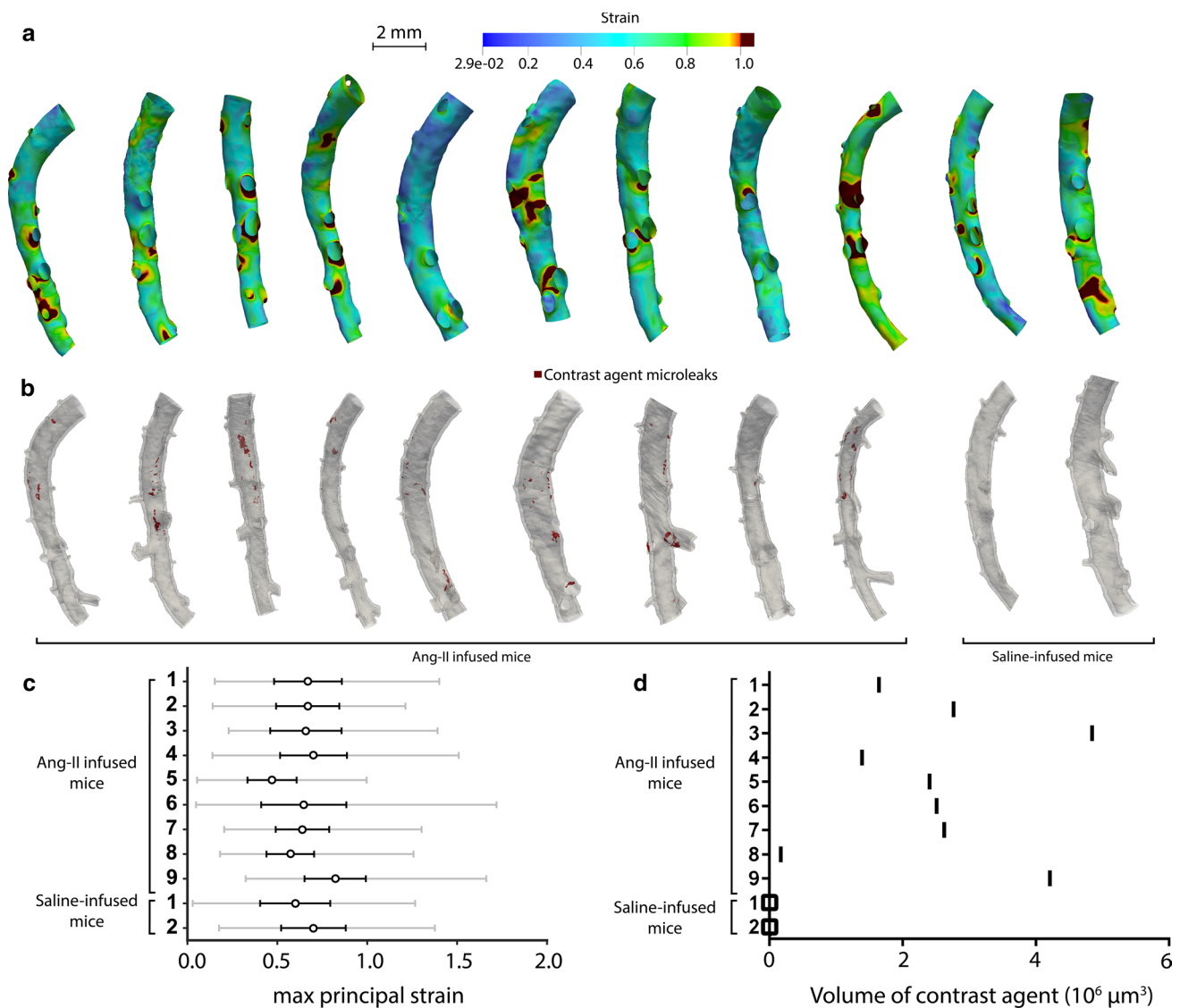
**Fig. 3 a** Structural FEM simulations of 9 AngII-infused and 2 saline-infused murine abdominal aortas. The strain contour plot was projected back onto the ex vivo undeformed configuration to enable direct comparisons of strain concentrations and contrast agent microleaks in the aortic wall. **b** 3D aortic wall renderings corresponding to geometries presented in A with contrast agent microleaks shown in red. **c** Error bar plot of principal strain. The thick black line shows the mean ± SD. Gray line shows range of strain values from minimum to maximum. **d** A scatter plot shows total volume of infiltrated contrast agent per aorta

For AngII-infused mice, the aortic zone around the first pair of intercostal arteries cranial to the celiac artery had significantly higher strain than the control mice (Fig. 4a, bottom). The volume of contrast agent in the vicinity of the (i) celiac artery and (ii) superior mesenteric and right renal artery was significantly higher than in corresponding regions in saline-infused mice ($P = 0.00001$ and $P = 0.0002$ respectively, Fig. 4b bottom). Moreover, the aortic region around the celiac artery had more extensive microleaks of contrast agent than did the zone around the left renal artery ($P = 0.0419$). No contrast agent was found in 67% of the straight regions, whereas this percentage dropped to 35% for the branching zones.

In order to compare regions of high strain to high contrast agent more directly, we plotted the high strain index versus contrast agent volume for all aortic segments, delineating between straight and branching regions (Fig. 5a, top and bottom, respectively). Most straight segments had low strain values, but among the clustered points around the origin of the axes some had nonzero contrast agent volumes. Discordant pairs—defined by predictions of low strain accompanied by high volumes of
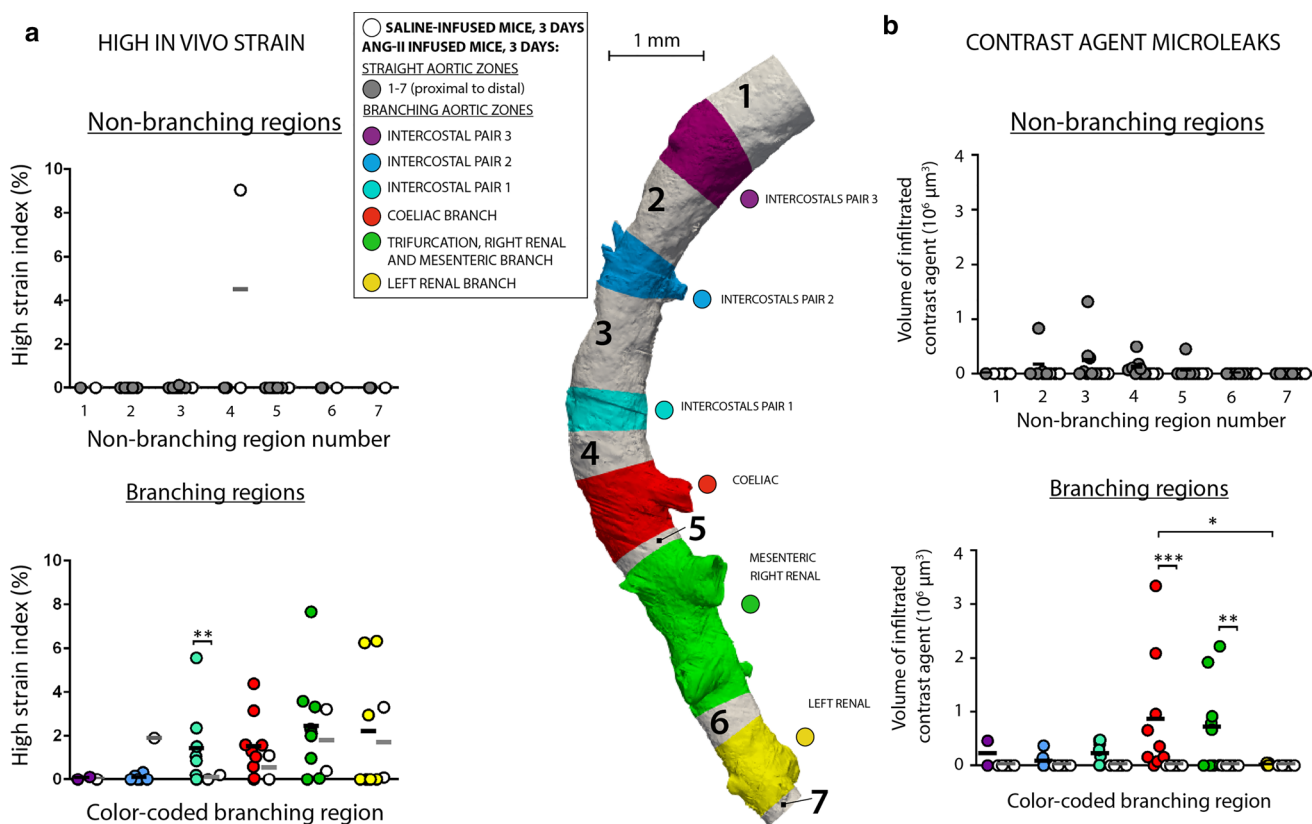
**Fig. 4** Center: color-coded division of the aorta in branching and straight zones. **a** Scatter plots show the computed high strain index (percentage of segment's surface area with strain values exceeding 80% of maximal strain) in straight and branching aortic regions in AngII-infused ($n=9$) and saline-infused ($n=2$) animals. **b** Scat-

ter plots show the volume of infiltrated contrast agent in straight and branching aortic regions in AngII-infused and saline-infused animals. Bold horizontal lines denote the mean of each group; gray lines denote the mean for saline-infused animals. *$P<0.05$, **$P<0.001$, ***$P<0.0001$
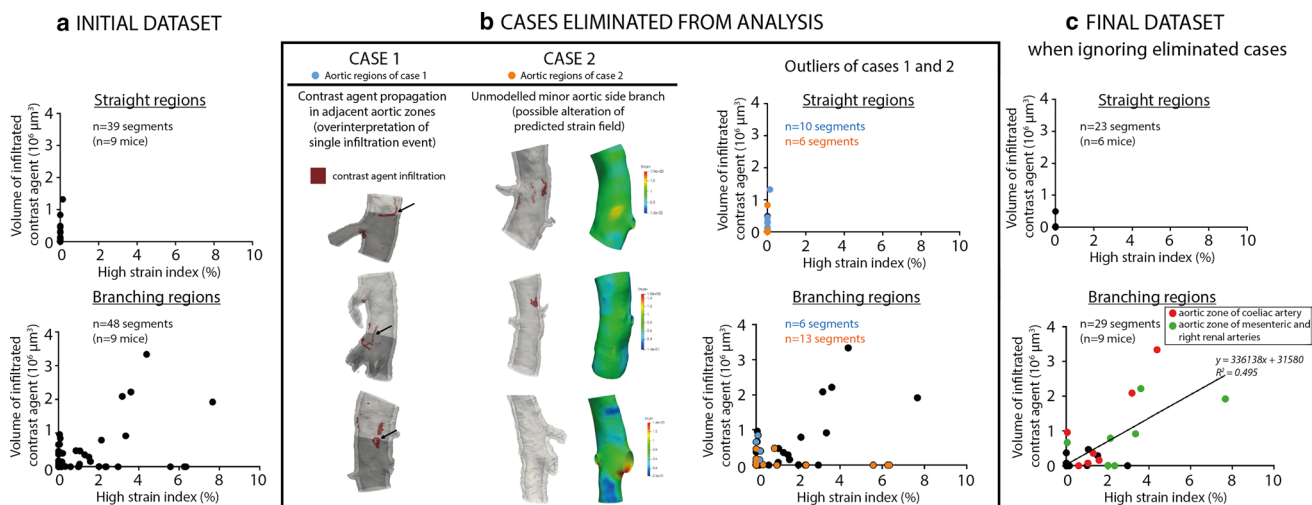


**Fig. 5** **a** Scatter plots show the correlation between high strain calculation and volume of contrast agent infiltration for straight and branching segments. **b** Outlier cases 1 and 2 were eliminated from the analysis (left) and color-coded on the scatter plots (right). The number of segments classified as case 1 (18% of all segments) or case 2

(22% of all segments) is in blue and orange, respectively. **c** Final scatter plots with data from cases 1 and 2 excluded from the analysis. For branching regions (bottom), color-coded data denote aortic regions (red for celiac artery region, green for superior mesenteric/right renal artery region)

contrast agent and vice versa—were found among branching regions as well. Upon closer examination of these cases, however, we found that most could be classified in one of two categories (Fig. 5b, cases 1 and 2). First, in a number of cases, the cutting planes used to partition the aortic geometry into segments intercepted a continuous volume of contrast agent that extended between two consecutive zones. This infiltrated volume resulted from the propagation of a single initial microleak (one point of entry) in the vessel wall. Thus, identifying two neighboring segments with a continuous volume of contrast agent as contrast agent-positive potentially led to an overestimation of the number of damage events suffered by the aortic wall. Second, in a number of cases, a minor aortic branch visualized on the PCXTM images was excluded in the FEM simulation due to difficulties in implementing the morphing framework. Omission of the side branches could have altered (either over- or underestimated) the computed local strain, as previously shown (Ferraro et al. 2018). In Fig. 5b, the data belonging to the aforementioned cases have been color-coded for straight (top) and branching regions (bottom). After eliminating them from the analysis, no significant correlation was found between high strain and contrast agent infiltration for straight segments (Fig. 5c, top). Conversely, a significant positive correlation between high strain and contrast agent volume emerged for branching segments (Fig. 5c bottom, $P < 0.0001$ with Pearson's correlation). These branching regions are color-coded, and the data driving the correlation arise mainly from the celiac and superior mesenteric/right renal arteries.

## 3.4 Circumferential distribution of contrast agent and strain around branch arteries

In order to assess circumferential variations in strain and vascular damage, and their relation to one another, we divided the most affected aortic segments—including the celiac branching region and superior mesenteric/right renal branching region—into four quadrants (Fig. 6, right). Both the volume of contrast agent and the computed strain were significantly higher in the ventral than in the dorsal aorta (Kruskal–Wallis test with post hoc Dunn's test for multiple comparisons, $P = 0.0008$ and $P = 0.0164$). The strain was also significantly higher in the ventral quadrant than in the left quadrant ($P = 0.0128$). A significant positive correlation was observed between ventral high strain index and ventral contrast agent accumulation (Fig. 6c, $P = 0.0191$).

## 3.5 Load-induced intramural delaminations ex vivo: the role of side branches

PCXTM-based 3D representations of four aortic samples that underwent ex vivo biaxial mechanical testing and presented with intramural delaminations can be seen in Fig. 7a–c. In all four samples, small side branches were damaged within the delaminated regions. The number of ruptured branches as well as the total number of branches found within the delaminated region of each sample is summarized in Table 2. Medial tears—defined as discontinuities of the tunica media across all elastic lamellae—were found in the vicinity of a side branch in the suprarenal and infrarenal aortas (Fig. 7d, zoomed panels). The celiac artery was the branch around which the medial tear appeared in the only sample that included

**Fig. 6** Scatter plots showing **a** the volume of contrast agent microleaks and **b** computed high strain variations along the circumference of the aortic region extending from the celiac to the right renal artery (quadrants as shown on right side). Bold horizontal line denotes mean value. $*P < 0.05$, $**P < 0.001$
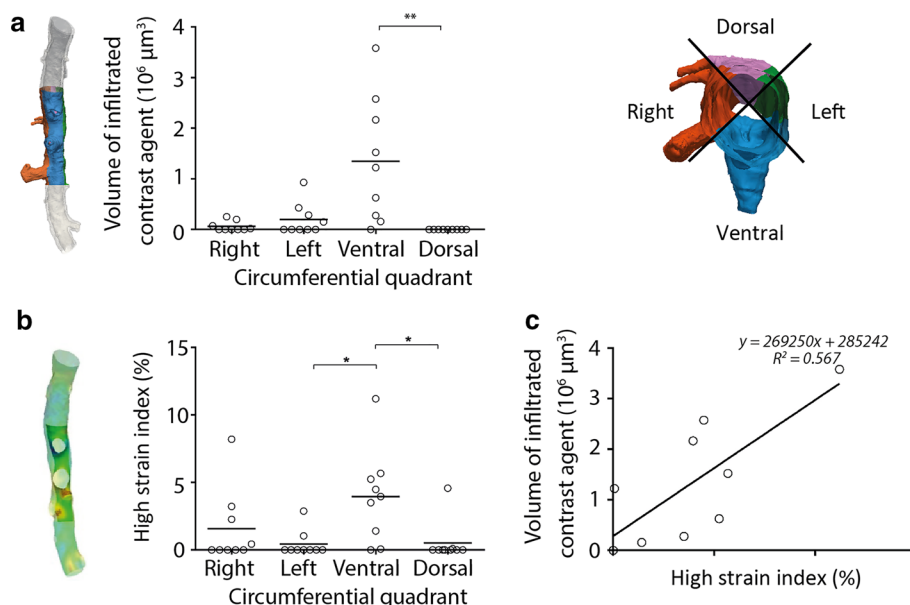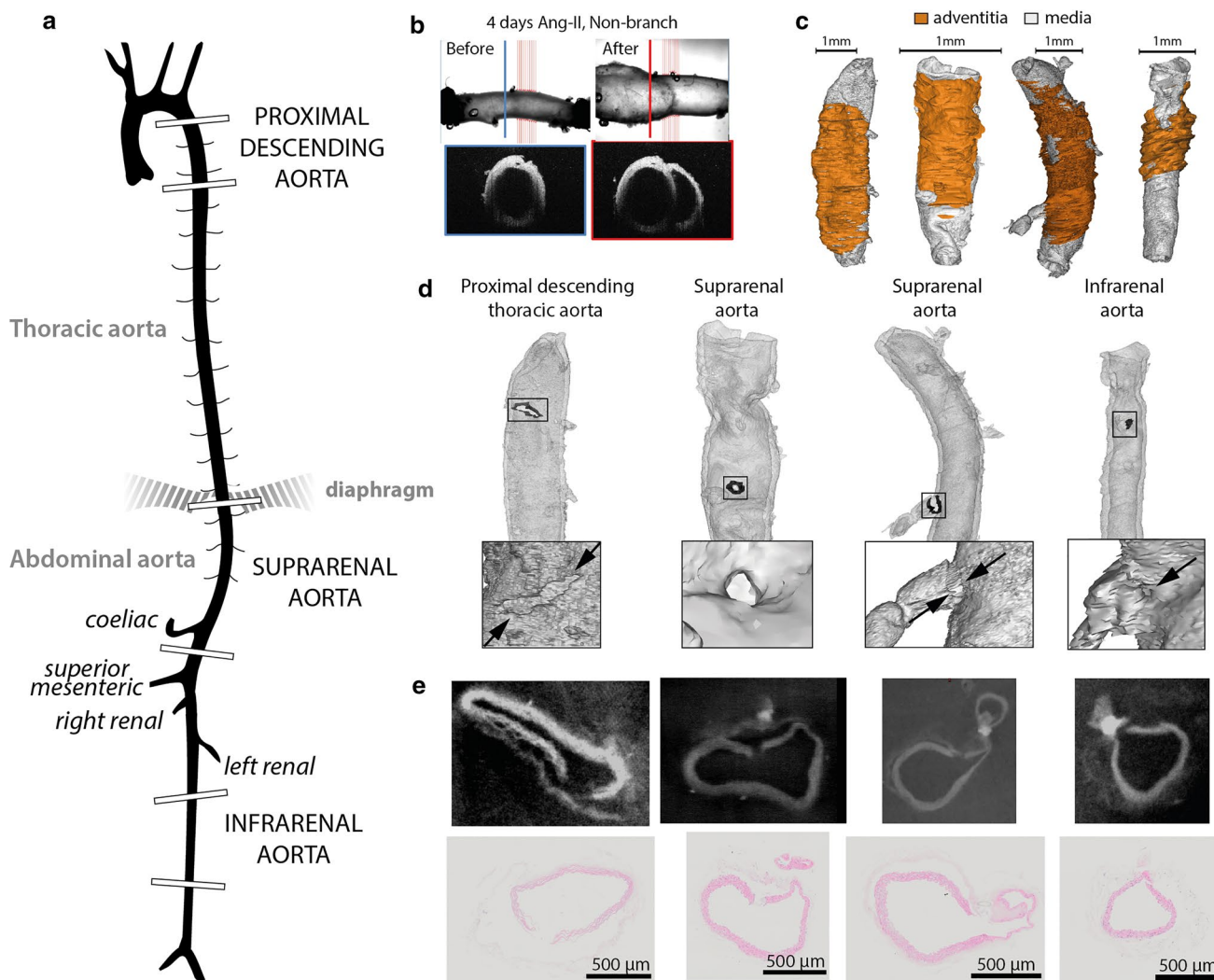
**Fig. 7 a** Illustration of the aortic regions for the four ex vivo tested samples. **b** Aortic delamination of the suprarenal aorta after 4 days of AngII infusion. Optical coherence tomography during biaxial mechanical testing shows spontaneous delamination of medial and adventitial layers. **c** 3D representations of the four samples that were subsequently scanned with PCXTM. The separated adventitial layer is shown in orange. **d** 3D representations of the media (adventitia not shown). Zoomed images show the major medial tear for each sample. **e** PCXTM images and targeted H&E histology in the locations of major medial tears shown in **d**

**Table 2** Quantification of ruptured and total side branches found within the delaminated region of four aortic samples subjected to ex vivo biaxial testing

| Sample | Aortic region | Total number of branches | Ruptured branch ostia (% of total branches) |
|--------|---------------|--------------------------|---------------------------------------------|
| 1 | Proximal descending thoracic aorta | 7 | 3 (43%) |
| 2 | Suprarenal abdominal aorta | 8 | 6 (75%) |
| 3 | Suprarenal abdominal aorta | 6 | 4 (67%) |
| 4 | Infrarenal aorta | 5 | 2 (40%) |

this ramification. In the proximal descending aorta, the major delamination plane was found in a non-branching region (Fig. 7d). All delaminations were contiguous with a ruptured or unruptured side branch. Correlative histology validated the observations of the 3D PCXTM images (Fig. 7e).

## 4 Discussion

To the best of our knowledge, this study is the first to use synchrotron-based biomechanics to predict in vivo aortic strains and to correlate strain concentrations with mouse-specific 3D intramural histopathology in the abdominal aorta. Toward this end, we used a common animal model of aortic dissection, the AngII-infused ApoE-deficient mouse (Trachet et al. 2017). Histopathological findings were similar to those reported by others. There was an early cellular infiltration in the subintimal, accumulation of macrophages in the media, and evident hematoma in the outer lamellar units in the suprarenal aorta of the AngII-infused mice, but a lack of overt morphological or histopathological changes in the aortas of saline-infused animals (Goergen et al. 2010; Saraff et al. 2003). There was also protection of the infrarenal aorta from pathological findings (Bersi et al. 2017).

### 4.1 Contrast agent as a surrogate marker for precursor vascular injury

We first confirmed that infiltration of an intravenously injected micro-CT contrast agent into the aortic lumen co-localizes with vascular damage. Comparative histology showed that this contrast agent served as a reliable indicator of vascular damage in 88% of the histological sections examined (Fig. 2c). Regarding the preferential detection of certain wall defects over others, we found that contrast agent infiltration is better suited to detect subintimal cellular infiltration and intramural hematoma, but less so the loss of medial VSMCs. Moreover, localization of infiltrated contrast agent, combined with an ability to measure its distribution noninvasively in full 3D datasets, provides an added advantage that arduous, arbitrarily located 2D histology cannot achieve. Thus, we submit that the 3D distribution of contrast infiltration along the aorta is a suitable alternative to certain aspects of 2D histology for the purpose of computational validation.

### 4.2 Initiating events in AngII-induced abdominal pathology: branching sites are biomechanically vulnerable

Aortic dissections occur almost exclusively in the suprarenal abdominal aorta in the AngII infusion model (Cao et al. 2010) and typically present within 3–10 days after the onset of AngII administration (Daugherty and Cassis 2004). Telemetric blood pressure assessment shows that the mice experience a +25 mmHg rise in mean blood pressure within 24 h from the onset of AngII infusion, with pressure increasing continuously to +31 mmHg at 3 days of infusion (Haggerty et al. 2015). Elevated blood pressure can differentially increase wall stress in the media and adventitia (Bellini et al. 2014), and it is expected that wall damage occurs when

wall stress exceeds wall strength. Within 24 h after dissection, neutrophil accumulation is much more pronounced than macrophage infiltration and very little collagen has yet to be deposited despite focal elastin breakage in the media (Phillips et al. 2018). It has been suggested that cellular targets of AngII also exert injurious effects to the aortic wall, independent of blood pressure (Cassis et al. 2009).

Using 2D histology, Gavish and colleagues identified transmedial disruptions at branch points in the abdominal aorta after 28 days of AngII infusion (Gavish et al. 2012, 2014). Using 3D synchrotron imaging, we subsequently observed similar microruptures in the tunica media after 28 days of infusion, not only near major but also near minor suprarenal side branches, and this without the need for serial sectioning (Trachet et al. 2014). Follow-up research revealed that medial defects already arise around the ostia of major and minor abdominal aortic side branches by 3 days of AngII infusion, thus suggesting involvement in initiation, not just outcome (Trachet et al. 2017). In addition to revealing local sites of intramural damage, we have shown that ex vivo synchrotron-based imaging can be combined with in vivo micro-CT-based imaging to provide geometric and kinematic information sufficient for informing biomechanical calculations of mean strain fields along the mouse aorta (Ferraro et al. 2018). In the present study we (i) validated our synchrotron-based biomechanics in a unique preclinical setting and (ii) investigated the role of biomechanics in disease initiation after only 3 days of AngII infusion, when lesions begin to form. As expected, we found that branching regions act as geometric and material discontinuities that can give rise to strain hotspots and sites of precursor vascular damage (Fig. 4). That is, a positive correlation was found between high mechanical strain and contrast agent infiltration in branching, but not in straight, regions of the suprarenal aorta (Fig. 5c). These findings thus support further the importance of side branches in the initiation of aortic dissection in mice resulting from AngII infusion (Gavish et al. 2014).

Due to the correlative nature of our experiments, we cannot establish an unequivocal causal link between high mechanical strain and vascular damage. In order to establish such a link, we would need to estimate the mechanical strain using synchrotron biomechanics on a healthy mouse, then follow the same animal after 3 days of AngII infusion and compare sites of wall injury to locations of elevated mechanical strain. This is currently not technically feasible since PCXTM is an ex vivo technique and the animal is killed before the images are taken. Yet, the strain concentrations we observe at branching regions of control animals would be expected to increase markedly at high pressures (i.e., with pressure elevation due to AngII infusion), thus increasing the likelihood of vascular damage at these sites. Indeed, there does not appear to be sufficient mechano-adaptation of the aortic wall via increased matrix deposition within

the first 3 to 4 days of AngII infusion (Bersi et al. 2017; Laroumanie et al. 2018), hence leaving sites of high stress/strain potentially more vulnerable to mechanical damage. In the suprarenal aorta in particular, there is an early and persistent increase in elastically stored energy at systolic pressure after 4 days of AngII infusion that is consistent with an increased circumferential strain, which may arise due to an early increase in MMP13 expression in the absence of collagen synthesis (Bersi et al. 2017; Laroumanie et al. 2018). This concept is consistent with the suggestion by Gavish et al. (2014) that dissections occur when vulnerable sites are not reinforced properly by collagen remodeling. The present results suggest further that following the AngII-induced rise in blood pressure, the first intimal and intramural defects in the suprarenal aorta may nucleate at branch sites that constitute strain hotspots that precede vascular damage.

## 4.3 Dorsal protection and circumferential variation

AngII-induced lesions not only occur preferentially in the suprarenal aorta of the mouse, they also form on the left side of the suprarenal aorta (Adelsperger et al. 2018; Goergen et al. 2010; Xie et al. 2012). Several hypotheses have been offered to explain this circumferential specificity (Goergen et al. 2010, 2011), but a clear explanation remains wanting. Despite having the highest strain index values and the highest volumes of contrast agent infiltration of all branching regions, there was no evidence of significant microstructural damage or strain hotspots in the dorsal quadrant of the celiac and superior mesenteric/right renal segments (Fig. 6b). Mechanical protection of the dorsal aorta is consistent with the lower stored energy density computed in the dorsal compared to the ventral half of the healthy ApoE-deficient suprarenal aorta (Bersi et al. 2016) and the threefold lower expansion of the posterior compared to the anterior abdominal wall (Goergen et al. 2007). The posterior perivascular support of the aorta (De Wilde et al. 2016)—such as the dorsal musculature and spinal tethering—could also explain its mechanical shielding.

Another striking observation is that microstructural damage preferentially occurs on the ventral and left quadrants of the celiac and superior mesenteric/right renal aortic segment. Interestingly, these segments also experience high strain on the ventral and (to a lesser extent) right quadrants (Fig. 6)—the quadrants with prominent branch ostia. When it comes to strain and vascular damage, the ventral quadrants of the celiac and superior mesenteric/right renal segments thus seem to be at the highest risk. This may at first seem contradictory to previous findings, which point to medial tears in the left and ventral, but not in the right, quadrant (Trachet et al. 2017). It is important to note, however, the difference between initiation and propagation. Indeed, the propagation of microruptures into medial tears,

and the subsequent dissection of the left side of the tunica adventitia, may be driven by additional mechanical factors.

## 4.4 Hypothesis on tear propagation

We previously conjectured that medial microruptures, occurring after 3 days of AngII infusion around the celiac and superior mesenteric branches but sometimes at the ostia of intercostal or left renal arteries, constitute the initial insult to the aortic wall in this mouse model of dissection (Trachet et al. 2017). These microruptures subsequently propagate to form a medial tear, previously termed by Gavish and colleagues (Gavish et al. 2012, 2014) as a transmedial or transmural disruption and found after 4 weeks of AngII infusion in the vicinity of the orifices of major abdominal branches. This theory is not in conflict with our current findings, which suggest that microruptures may form in locations that experience the highest strain and then propagate to form larger medial defects. We further hypothesized that the transition from microrupture to medial tear is dictated by the local mechanics near the small side branches, which may or may not be torn as the medial tear propagates in the aorta.

This general concept is supported further by the synchrotron-based images of spontaneous delaminations that occurred in 4-day AngII-infused aortas during ex vivo biaxial testing (Fig. 7). Importantly, these vessels are tested in the absence of additional mechanical factors such as complex hemodynamics and perivascular support, hence allowing one to focus on discontinuities near branches. The medial tear that appeared to act as an entry point for saline to enter between media and adventitia was found near a side branch for the suprarenal and infrarenal aortas, specifically around the celiac artery in the sample that included this bifurcation (sample 3). Moreover, all of the delaminations observed ex vivo coincided with small side branches, suggesting that the latter may have acted as originating sites or anchoring points to sustain the propagating delamination. Though we do not know whether these samples would have progressed to aortic dissection in vivo had they not been harvested at 4 days, our ex vivo observations suggest that the use of precisely controlled supra-physiological loading conditions in the absence of in vivo perivascular support may reveal an intrinsic predisposition to strain-induced delamination at branch sites following AngII infusion.

## 4.5 Limitations and future work

Our validation of contrast agent as an indicator of future vascular damage yielded a modest number of false positives and false negatives ($\leq 6\%$ of all measurements; Fig. 2c). Nevertheless, these mismatches between contrast agent

and histopathological lesion presence constitute a potential source of uncertainty. It is important to emphasize, however, that histological preparations inherently induce cutting artifacts, particularly in structurally vulnerable samples and mismatches can occur due to errors in mapping histological slides to the corresponding ex vivo synchrotron image. Hence, using infiltrating contrast agent as an in vivo marker of vulnerability is promising.

We used a custom semiautomated morphing framework to compute the in vivo strain field of murine abdominal aortas. This framework combines ex vivo PCXTM and in vivo micro-CT to provide morphological information on local axial stretch, minor aortic side branches, and mouse-specific aortic wall thickness. A sensitivity analysis shows that all of these features can significantly alter the computed strain hotspots in the FEM simulations (Ferraro et al. 2018) and are thus critical to measure. Some limitations of the framework have been described previously, and include (among others) shrinkage of the sample due the dehydrating fixation process for the PCXTM, the absence of pre-stress, and the use of a simplistic material model (Ferraro et al. 2018). Additional limitations of our morphing approach include the assumption of material homogeneity (which disregards possible mechanical homeostasis near branches) and the difficulty of modeling small side branches or a collapsed aortic geometry. Due to problems with collapsed (non-pressured) geometries—leading to poor mesh element quality—we were unable to model four cases of saline-infused animals and 1 case of an AngII-infused mouse (Appendix Fig. 8). A similar problem did not arise for the rest of the AngII-infused vessels, which appeared to be structurally stiffer. The impact of this work would have been greater had we managed to include more saline-infused control cases. We were also not able to model some of the smallest branches, which may have influenced the results (Fig. 5b).

In the context of computational–experimental studies, more sophisticated approaches have been proposed for identifying correlations between indices of hemodynamic simulations and plaque-related damage (De Wilde et al. 2016). We did not implement such approaches here because we did not expect to find an exact match between voxels with high strain and voxels with contrast agent infiltration. Indeed, our synchrotron images do not allow an unequivocal determination of the point of entry of contrast agent into the wall. Upon entering the wall, contrast agent can spread due to the transmural pressure gradient and diffusion. The choice for larger, branch- versus straight-segment defined regions thus allowed more robust comparisons. In this context, it is important that our post-hoc outlier removal (Fig. 5b) was based on clear criteria—binary variables of presence/absence of contrast agent and aortic side branches—that were not subject to interpretation, thus avoiding observer bias.

Finally, it has been postulated that non-uniform distributions of collagen fiber orientation near branch sites lead to local material heterogeneities that could generate intramural shear stresses sufficient to initiate a delamination event which subsequently propagates into a dissection (Bellini et al. 2017). Such effects were not considered in our current modeling and simulation strategy. Conversely, studies on porcine aortas have recently suggested that a strain-driven collagen fiber rearrangement mechanism may exist (Gaul et al. 2018). In the future work, we intend to extend our current methodology to include more sophisticated imaging and material models that account for local fiber orientation. This might also allow us to gain a better understanding of the role of biomechanics in the regional variations in contrast agent infiltration that was observed within the AngII-infused group (Fig. 2d). More sophisticated material models will also allow better computations of wall stress, not just wall strain, noting that it is yet unknown whether intramural damage leading to dissection or rupture follow a stress-, strain-, or energy-based failure criterion. Correlations of damage with strain have the added advantage, however, of potential measurement without detailed understanding of the evolving, likely anisotropic and heterogeneous material properties.

## 5 Conclusions

We have used synchrotron-based biomechanics to study initiating events in the AngII infusion mouse model of aortic dissection. We predicted in vivo aortic strains and correlated strain concentrations with mouse-specific 3D histopathological defects in the abdominal aortas of AngII-infused mice. We submit that branching sites sustain significantly higher strain and wall injury compared to non-branching regions, and that the dorsal aorta is mechanically protected. Ex vivo load-induced aortic delaminations further point toward branching regions as nucleating sites for aortic dissections in AngII-infused mice.

## Appendix

See Fig. 8.

**Fig. 8** Collapsed geometries in undeformed configurations for $n = 4$ saline-infused and $n = 1$ AngII-infused mice



Saline-infused controls     Ang II-infused
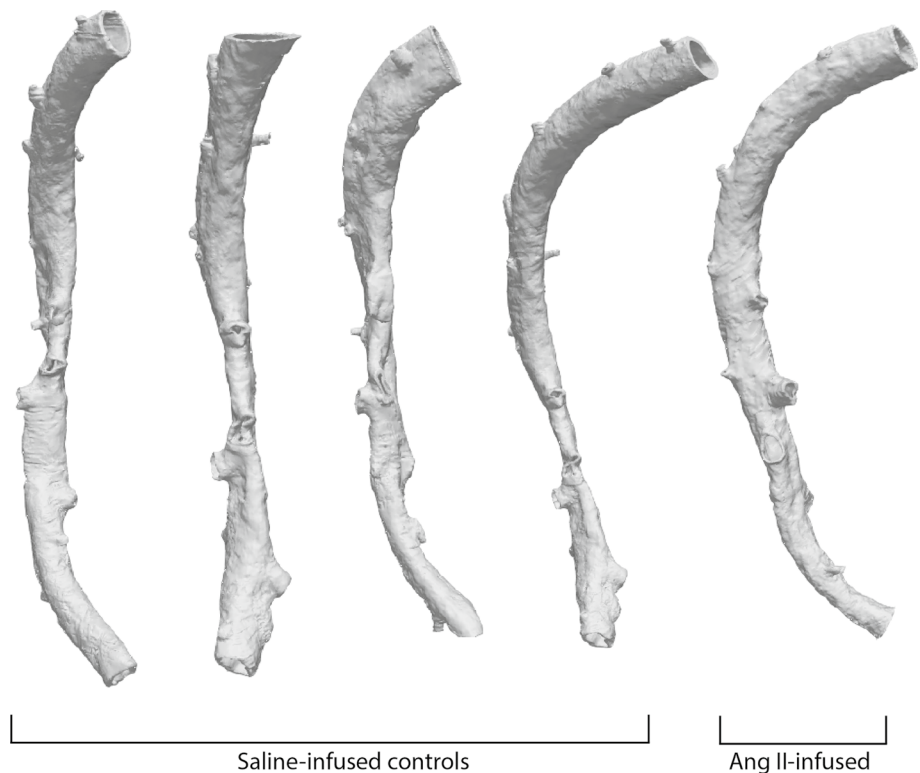
# References

Adelsperger AR, Phillips EH, Ibriga HS, Craig BA, Green LA, Murphy MP, Goergen CJ (2018) Development and growth trends in angiotensin II-induced murine dissecting abdominal aortic aneurysms. Physiol Rep 6:e13668. https://doi.org/10.14814/phy2.13668

Ayachit U (2015) The paraview guide: a parallel visualization application. Kitware Inc, New York

Bellini C, Ferruzzi J, Roccabianca S, Di Martino ES, Humphrey JD (2014) A microstructurally motivated model of arterial wall mechanics with mechanobiological implications. Ann Biomed Eng 42:488–502. https://doi.org/10.1007/s10439-013-0928-x

Bellini C, Kristofik NJ, Bersi MR, Kyriakides TR, Humphrey JD (2017) A hidden structural vulnerability in the thrombospondin-2 deficient aorta increases the propensity to intramural delamination. J Mech Behav Biomed Mater 71:397–406. https://doi.org/10.1016/j.jmbbm.2017.01.045

Bersi MR, Bellini C, Di Achille P, Humphrey JD, Genovese K, Avril S (2016) Novel methodology for characterizing regional variations in the material properties of murine aortas. J Biomech Eng 138:071005. https://doi.org/10.1115/1.4033674

Bersi MR, Khosravi R, Wujciak AJ, Harrison DG, Humphrey JD (2017) Differential cell-matrix mechanoadaptations and inflammation drive regional propensities to aortic fibrosis, aneurysm or dissection in hypertension. J R Soc Interface 14:20170327

Bonfanti M, Balabani S, Greenwood JP, Puppala S, Homer-Vanniasinkam S, Díaz-Zuccarini V (2017) Computational tools for clinical support: a multi-scale compliant model for haemodynamic simulations in an aortic dissection based on multi-modal imaging data. J R Soc Interface 14:20170632

Cao RY, Amand T, Ford MD, Piomelli U, Funk CD (2010) The murine angiotensin II-induced abdominal aortic aneurysm model: rupture risk and inflammatory progression patterns. Front Pharmacol 1:9. https://doi.org/10.3389/fphar.2010.00009

Cassis LA et al (2009) ANG II infusion promotes abdominal aortic aneurysms independent of increased blood pressure in hypercholesterolemic mice. Am J Physiol Heart Circ Physiol 296:H1660–H1665. https://doi.org/10.1152/ajpheart.00028.2009

Chen HY et al (2016) Editor's choice—fluid-structure interaction simulations of aortic dissection with bench validation. Eur J Vasc Endovasc Surg 52:589–595. https://doi.org/10.1016/j.ejvs.2016.07.006

Chi Q, He Y, Luan Y, Qin K, Mu L (2017) Numerical analysis of wall shear stress in ascending aorta before tearing in type A aortic dissection. Comput Biol Med 89:236–247. https://doi.org/10.1016/j.compbiomed.2017.07.029

Daugherty A, Cassis LA (2004) Mouse models of abdominal aortic aneurysms. Arterioscler Thromb Vasc Biol 24:429–434. https://doi.org/10.1161/01.atv.0000118013.72016.ea

Daugherty A, Manning MW, Cassis LA (2000) Angiotensin II promotes atherosclerotic lesions and aneurysms in apolipoprotein E–deficient mice. J Clin Investig 105:1605–1612. https://doi.org/10.1172/jci7818

De Wilde D, Trachet B, De Meyer GRY, Segers P (2016) Shear stress metrics and their relation to atherosclerosis: an in vivo follow-up study in atherosclerotic mice. Ann Biomed Eng 44:2327–2338. https://doi.org/10.1007/s10439-015-1540-z

Farotto D, Segers P, Meuris B, Vander Sloten J, Famaey N (2018) The role of biomechanics in aortic aneurysm management: requirements, open problems and future prospects. J Mech Behav Biomed Mater 77:295–307. https://doi.org/10.1016/j.jmbbm.2017.08.019

Favreau JT et al (2012) Murine ultrasound imaging for circumferential strain analyses in the angiotensin II abdominal aortic aneurysm model. J Vasc Surg 56:462–469. https://doi.org/10.1016/j.jvs.2012.01.056

Ferraro M, Trachet B, Aslanidou L, Fehervary H, Segers P, Stergiopulos N (2018) Should we ignore what we cannot measure? How non-uniform stretch, non-uniform wall thickness and minor side branches affect computational aortic biomechanics in mice. Ann Biomed Eng 46:159–170. https://doi.org/10.1007/s10439-017-1945-y

Ferruzzi J et al (2016) Pharmacologically improved contractility protects against aortic dissection in mice with disrupted transforming growth factor-β signaling despite compromised extracellular matrix properties. Arterioscler Thromb Vasc Biol 36:919–927. https://doi.org/10.1161/atvbaha.116.307436

Ferruzzi J, Di Achille P, Tellides G, Humphrey JD (2018) Combining in vivo and in vitro biomechanical data reveals key roles of perivascular tethering in central artery function. PLoS ONE 13:e0201379. https://doi.org/10.1371/journal.pone.0201379

Ford MD, Black AT, Cao RY, Funk CD, Piomelli U (2011) Hemodynamics of the mouse abdominal aortic aneurysm. J Biomech Eng 133:121008–121009. https://doi.org/10.1115/1.4005477

Gaul RT, Nolan DR, Lally C (2018) The use of small angle light scattering in assessing strain induced collagen degradation in arterial tissue ex vivo. J Biomech 81:155–160. https://doi.org/10.1016/j.jbiomech.2018.10.006

Gavish L et al (2012) Low level laser arrests abdominal aortic aneurysm by collagen matrix reinforcement in apolipoprotein E-deficient mice. Lasers Surg Med 44:664–674. https://doi.org/10.1002/lsm.22068

Gavish L et al (2014) Inadequate reinforcement of transmedial disruptions at branch points subtends aortic aneurysm formation in apolipoprotein-E-deficient mice. Cardiovasc Pathol 23:152–159. https://doi.org/10.1016/j.carpath.2013.12.005

Genovese K, Collins MJ, Lee YU, Humphrey JD (2012) Regional finite strains in an angiotensin-II induced mouse model of dissecting abdominal aortic aneurysms. Cardiovasc Eng Technol 3:194–202. https://doi.org/10.1007/s13239-012-0083-9

Goergen CJ, Johnson BL, Greve JM, Taylor CA, Zarins CK (2007) Increased anterior abdominal aortic wall motion: possible role in aneurysm pathogenesis and design of endovascular devices. J Endovasc Therapy 14:574–584. https://doi.org/10.1177/152660280701400421

Goergen CJ et al (2010) In vivo quantification of murine aortic cyclic strain, motion, and curvature: implications for abdominal aortic aneurysm growth. J Magn Reson Imaging 32:847–858. https://doi.org/10.1002/jmri.22331

Goergen CJ et al (2011) Influences of aortic motion and curvature on vessel expansion in murine experimental aneurysms. Arterioscler Thromb Vasc Biol 31:270–279. https://doi.org/10.1161/atvbaha.110.216481

Haggerty CM, Mattingly AC, Gong MC, Su W, Daugherty A, Fornwalt BK (2015) Telemetric blood pressure assessment in angiotensin II-Infused apoe-/- mice: 28 day natural history and comparison to tail-cuff measurements. PLoS ONE 10:e0130723. https://doi.org/10.1371/journal.pone.0130723

Humphrey JD, Holzapfel GA (2012) Mechanics, mechanobiology, and modeling of human abdominal aorta and aneurysms. J Biomech 45:805–814. https://doi.org/10.1016/j.jbiomech.2011.11.021

Laroumanie F et al (2018) LNK deficiency promotes acute aortic dissection and rupture. JCI Insight 3:e122558. https://doi.org/10.1172/jci.insight.122558

Leemans EL, Willems TP, van der Laan MJ, Slump CH, Zeebregts CJ (2016) Biomechanical indices for rupture risk estimation in abdominal aortic aneurysms. J Endovasc Therapy 24:254–261. https://doi.org/10.1177/1526602816680088

Manopoulos C, Karathanasis I, Kouerinis I, Angouras DC, Lazaris A, Tsangaris S, Sokolis DP (2018) Identification of regional/layer differences in failure properties and thickness as important biomechanical factors responsible for the initiation of aortic dissections. J Biomech 80:102–110. https://doi.org/10.1016/j.jbiomech.2018.08.024

Nathan DP et al (2011) Pathogenesis of acute aortic dissection: a finite element stress analysis. Ann Thorac Surg 91:458–463. https://doi.org/10.1016/j.athoracsur.2010.10.042

Perrin D, Badel P, Orgeas L, Geindreau C, du Roscoat S, Albertini J-N, Avril S (2016) Patient-specific simulation of endovascular repair surgery with tortuous aneurysms requiring flexible stent-grafts. J Mech Behav Biomed Mater 63:86–99. https://doi.org/10.1016/j.jmbbm.2016.06.013

Phillips EH, Achille PD, Bersi MR, Humphrey JD, Goergen CJ (2017) Multi-modality imaging enables detailed hemodynamic simulations in dissecting aneurysms in mice. IEEE Trans Med Imaging 36:1297–1305. https://doi.org/10.1109/tmi.2017.2664799

Phillips EH, Lorch AH, Durkes AC, Goergen CJ (2018) Early pathological characterization of murine dissecting abdominal aortic aneurysms APL. Bioengineering 2:046106. https://doi.org/10.1063/1.5053708

Saraff K, Babamusta F, Cassis LA, Daugherty A (2003) Aortic dissection precedes formation of aneurysms and atherosclerosis in angiotensin II-infused, apolipoprotein E-deficient mice. Arterioscler Thromb Vasc Biol 23:1621–1626. https://doi.org/10.1161/01.atv.0000085631.76095.64

Sho E, Sho M, Nanjo H, Kawamura K, Masuda H, Dalman RL (2004) Hemodynamic regulation of CD34+ cell localization and differentiation in experimental aneurysms. Arterioscler Thromb Vasc Biol 24:1916–1921. https://doi.org/10.1161/01.atv.0000142805.20398.74

The Vascular Modeling Toolkit website, www.vmtk.org

Trachet B et al (2011) An integrated framework to quantitatively link mouse-specific hemodynamics to aneurysm formation in angiotensin II-infused Apoe −/− mice. Ann Biomed Eng 39:2430. https://doi.org/10.1007/s10439-011-0330-5

Trachet B et al (2014) Dissecting abdominal aortic aneurysm in Ang II-infused mice: suprarenal branch ruptures and apparent luminal dilatation. Cardiovasc Res 105:213–222. https://doi.org/10.1093/cvr/cvu257

Trachet B, Bols J, Degroote J, Verhegghe B, Stergiopulos N, Vierendeels J, Segers P (2015a) An animal-specific FSI model of the abdominal aorta in anesthetized mice. Ann Biomed Eng 43:1298–1309. https://doi.org/10.1007/s10439-015-1310-y

Trachet B, Fraga-Silva RA, Jacquet PA, Stergiopulos N, Segers P (2015b) Incidence, severity, mortality, and confounding factors for dissecting AAA detection in angiotensin II-infused mice: a meta-analysis. Cardiovasc Res 108:159–170. https://doi.org/10.1093/cvr/cvv215

Trachet B, Fraga-Silva RA, Piersigilli A, Segers P, Stergiopulos N (2015c) Dissecting abdominal aortic aneurysm in Angiotensin II-infused mice: the importance of imaging. Curr Pharm Des 21(28):4049–4060

Trachet B et al (2017) Angiotensin II infusion into ApoE-/- mice: a model for aortic dissection rather than abdominal aortic aneurysm? Cardiovasc Res 113:1230–1242. https://doi.org/10.1093/cvr/cvx128

Trachet B et al (2018) Synchrotron-based phase contrast imaging of cardiovascular tissue in mice—grating interferometry or phase propagation? Biomed Phys Eng Express 5:015010

Vorp DA (2007) Biomechanics of abdominal aortic aneurysm. J Biomech 40:1887–1902. https://doi.org/10.1016/j.jbiomech.2006.09.003

Wang Y-X et al (2001) Angiotensin II increases urokinase-type plasminogen activator expression and induces aneurysm in the abdominal aorta of apolipoprotein e-deficient mice. Am J Pathol 159:1455–1464. https://doi.org/10.1016/s0002-9440(10)62532-1

Xie X, Lu H, Moorleghen JJ, Howatt DA, Rateri DL, Cassis LA, Daugherty A (2012) Doxycycline does not influence established abdominal aortic aneurysms in angiotensin II-infused mice. PLoS ONE 7:e46411. https://doi.org/10.1371/journal.pone.0046411